

Electronic Supporting Information

Bioinspired selective synthesis of liquid-crystalline nanocomposites: formation of calcium carbonate-based composite nanodisks and nanorods

Masanari Nakayama, Satoshi Kajiyama, Akihito Kumamoto, Yuichi Ikuhara, Takashi Kato*

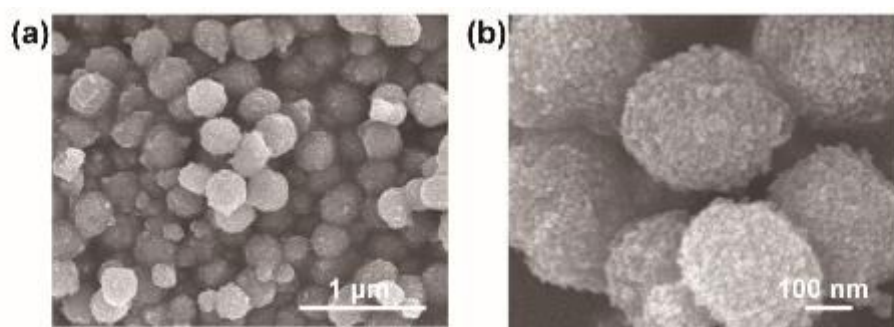


Fig. S1 Scanning electron microscopy (SEM) images of nanodisks at (a) low magnification and (b) high magnification.

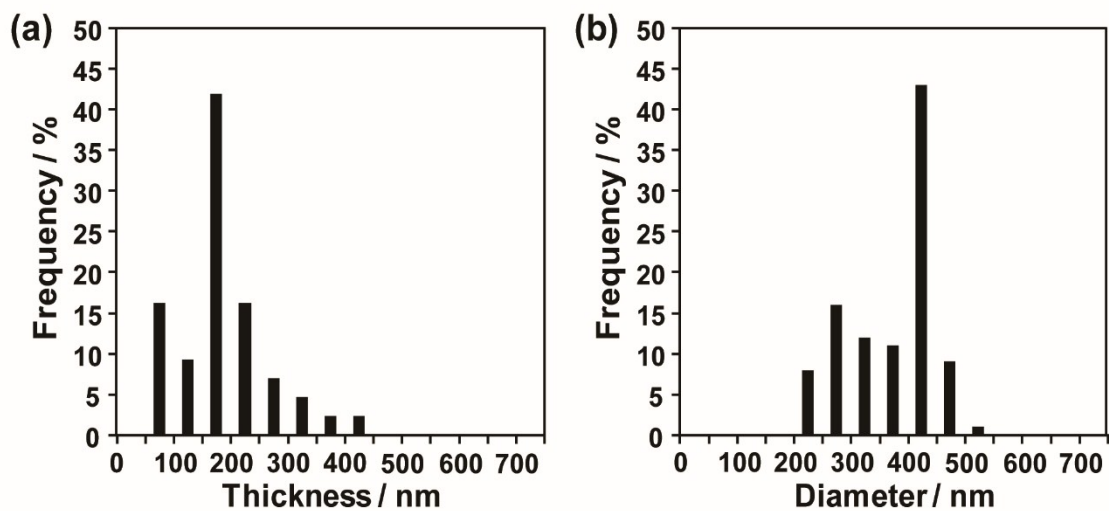


Fig. S2 Size distribution histograms of vaterite nanodisks after crystallization of the amorphous CaCO_3 (ACC) precursors in methanol/water (7:3) solution for (a) thickness and (b) diameter.

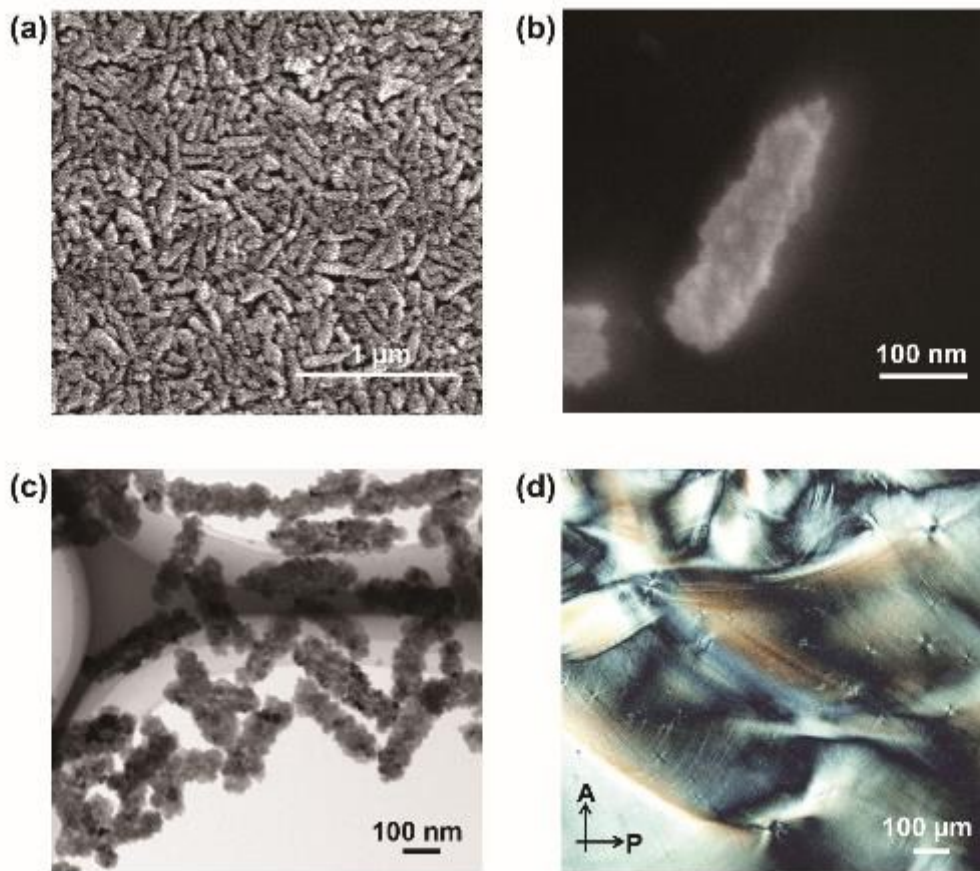


Fig. S3 SEM images of nanorods at (a) low magnification and (b) high magnification. (c) Transmission electron microscopy (TEM) image of nanorods. (d) Polarizing optical microscopy (POM) image of an aqueous colloidal dispersion of nanorods with a volume fraction of 30 vol%. A: Analyzer. P: Polarizer.

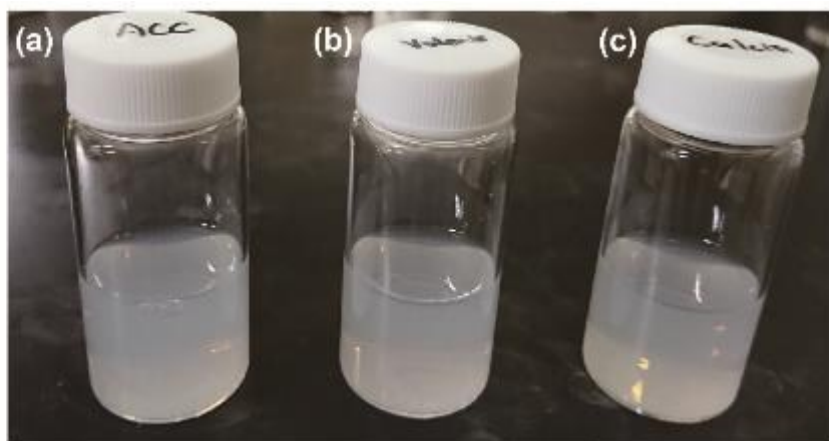


Fig. S4 Photographs of aqueous colloidal dispersions of (a) ACC precursors, (b) nanodisks, and (c) nanorods.

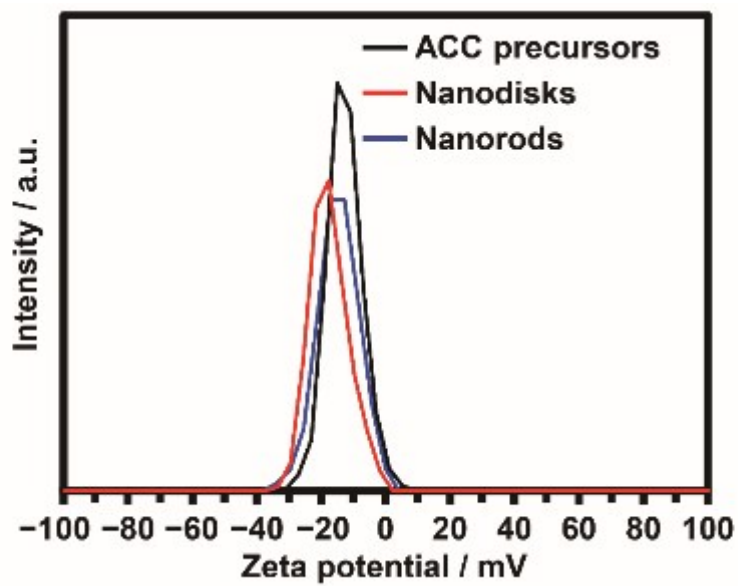


Fig. S5 Zeta potential curves for ACC precursors, nanodisks, and nanorods.

The average zeta potentials of ACC precursors, nanodisks, and nanorods were -12.7 ± 5 , -17.4 ± 6 , and -14.7 ± 6 mV, respectively.

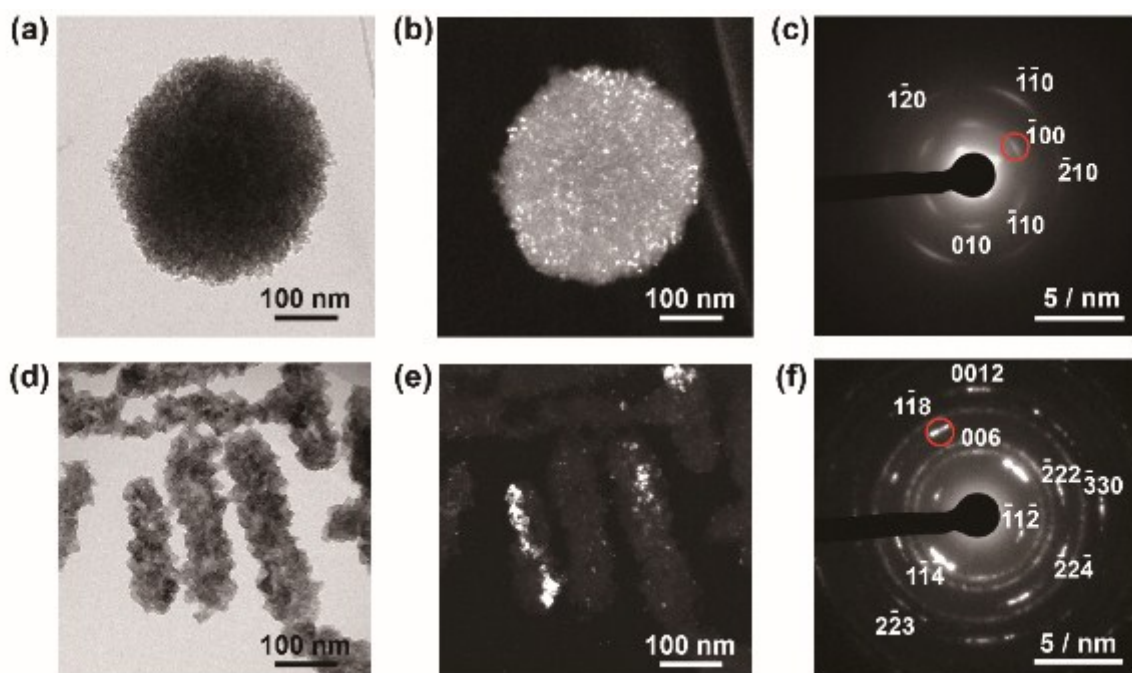


Fig. S6 (a) Bright-field TEM image of a nanodisk. (b) Dark-field TEM image corresponding to (a). (c) Selected-area electron diffraction (SAED) pattern corresponding to (a). The red circle indicates the area of the ($\bar{1}00$) reflection used for the dark-field observation in (b). (d) Bright-field TEM image of nanorods. (e) Dark-field TEM image corresponding to (d). (f) SAED pattern corresponding to (d). The red circle in (f) indicates the area of the ($\bar{1}18$) reflection used for the dark-field observation in (e).

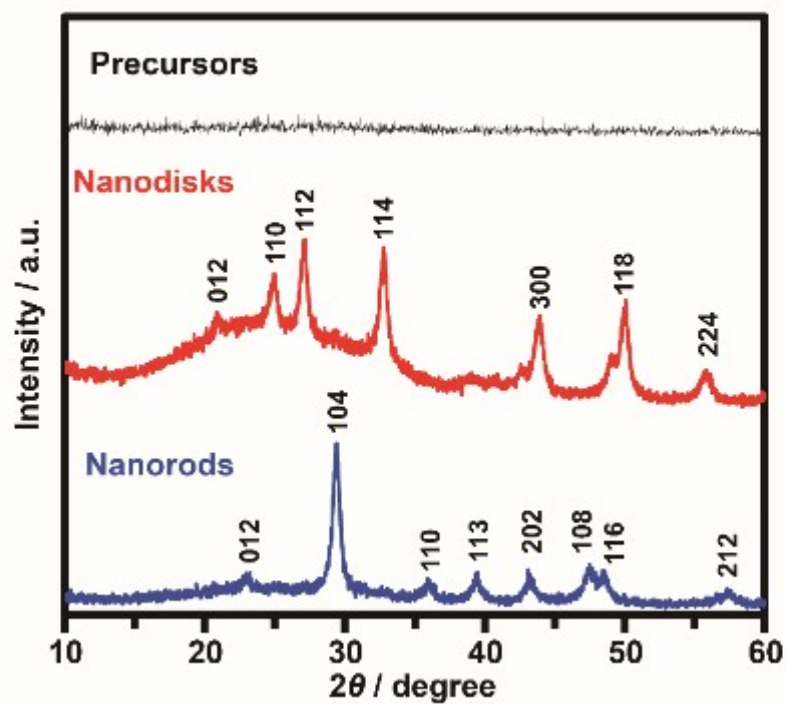


Fig. S7 X-ray diffraction (XRD) patterns obtained for amorphous precursors (top), nanodisks (middle), and nanorods (bottom).

No peak was observed in the XRD pattern of the precursors. All the peaks observed for the nanodisks were characteristic of vaterite, whereas the peaks observed for the nanorods were characteristic of calcite. For example, the characteristic peak of vaterite at $2\theta = 25.0^\circ$ corresponding to the (110) of vaterite was observed for nanodisks and the characteristic peak of calcite at $2\theta = 29.5^\circ$ corresponding to the (104) of calcite was observed for nanorods.¹

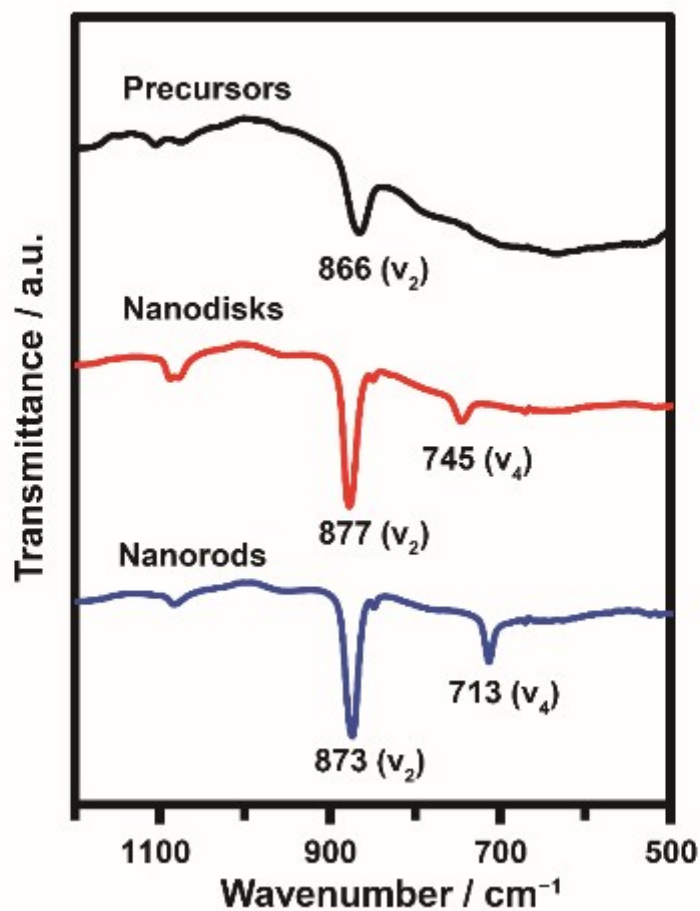


Fig. S8 Fourier-transform infrared (FTIR) spectra of ACC precursors (top), nanodisks (middle), and nanorods (bottom).

The peak at 866 cm⁻¹ for the precursors was assigned to the out-of-plane bending of CO₃²⁻ (ν₂) of ACC.² The peaks at 745 and 877 cm⁻¹ observed for the nanodisks were attributed to in-plane bending (ν₄) and out-of-plane bending (ν₂) of CO₃²⁻ of vaterite, respectively. The peaks at 713 and 873 cm⁻¹ observed for the nanorods were attributed to in-plane bending (ν₄) and out-of-plane bending (ν₂) of CO₃²⁻ of calcite, respectively.

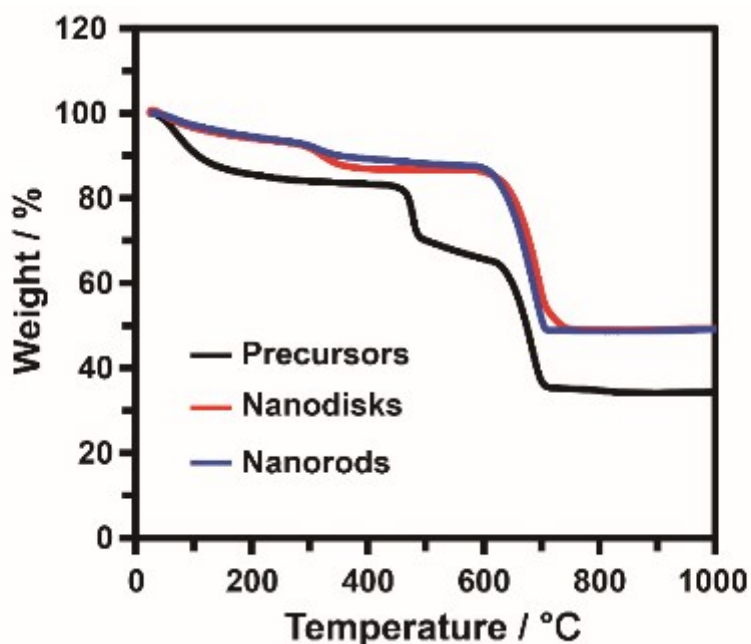


Fig. S9 Thermogravimetric (TG) curves obtained for ACC precursors, nanodisks, and nanorods.

It was previously reported that poly(acrylic acid) (PAA) molecules decompose at 200 to 600 °C and water molecules evaporate below 200 °C.³ Based on the previous report, the compositions of the samples were estimated. In the TG curves, the weight loss from 0 °C to 200 °C was calculated as the weight of water molecules, and the weight loss from 200 °C to 600 °C was calculated as the weight of PAA molecules. The remaining weight was calculated as the weight of CaCO₃. The composition of ACC precursors was 66 wt% CaCO₃, 20 wt% PAA, and 14 wt% H₂O. Nanodisks were composed of 86 wt% CaCO₃, 7.9 wt% PAA, and 6.1 wt% H₂O. Nanorods were composed of 87.0 wt% CaCO₃, 7.5 wt% PAA, and 5.5 wt% H₂O. These high values of PAA amounts suggest that PAA molecules exist not only on the surface but also between internal nanocrystallites of the vaterite nanodisks and calcite nanorods.

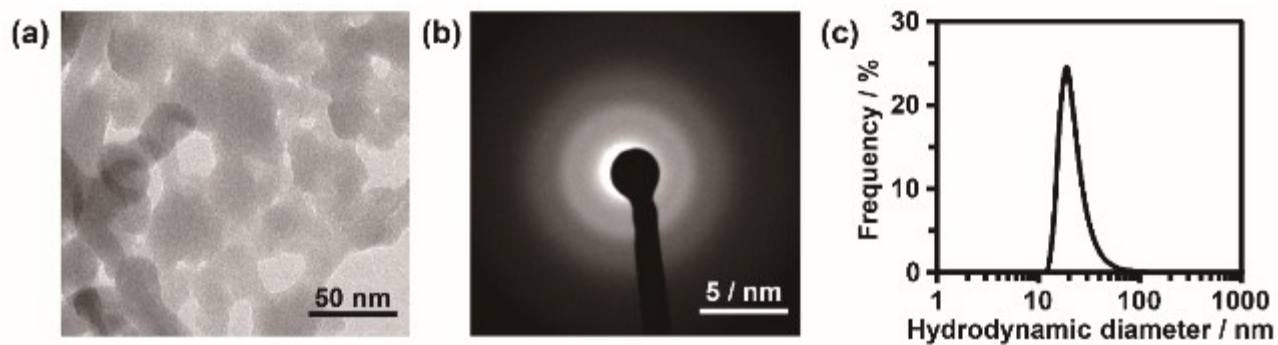


Fig. S10 (a) TEM image of ACC precursors, (b) corresponding SAED pattern, and (c) hydrodynamic diameter distribution of ACC precursors measured by dynamic light scattering.

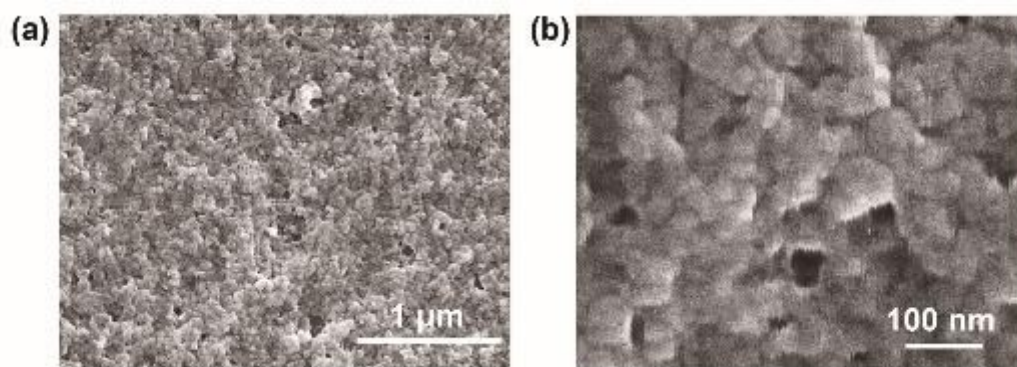


Fig. S11 SEM images of ACC precursors at (a) low magnification and (b) high magnification.

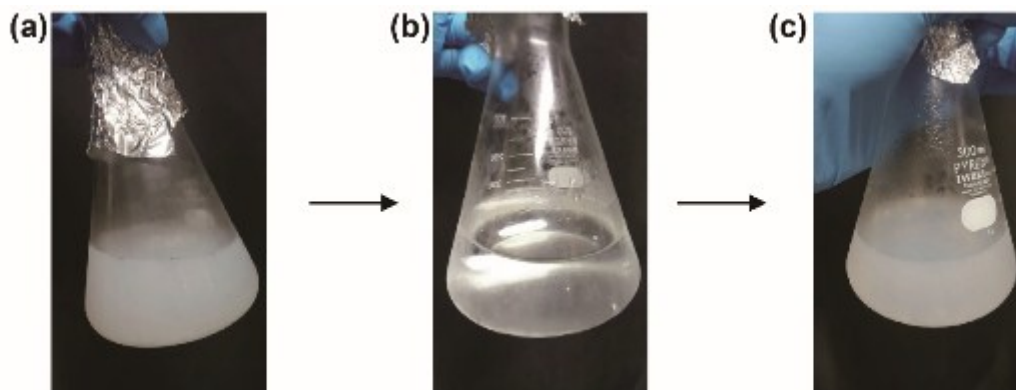


Fig. S12 Photographs of (a) an aqueous colloidal dispersion of ACC precursors before addition to 25 mM Na_2CO_3 aqueous solution, (b) 25 mM Na_2CO_3 aqueous solution 22 h after addition of the ACC precursors, and (c) 25 mM Na_2CO_3 aqueous solution 72 h after addition of the ACC precursors.

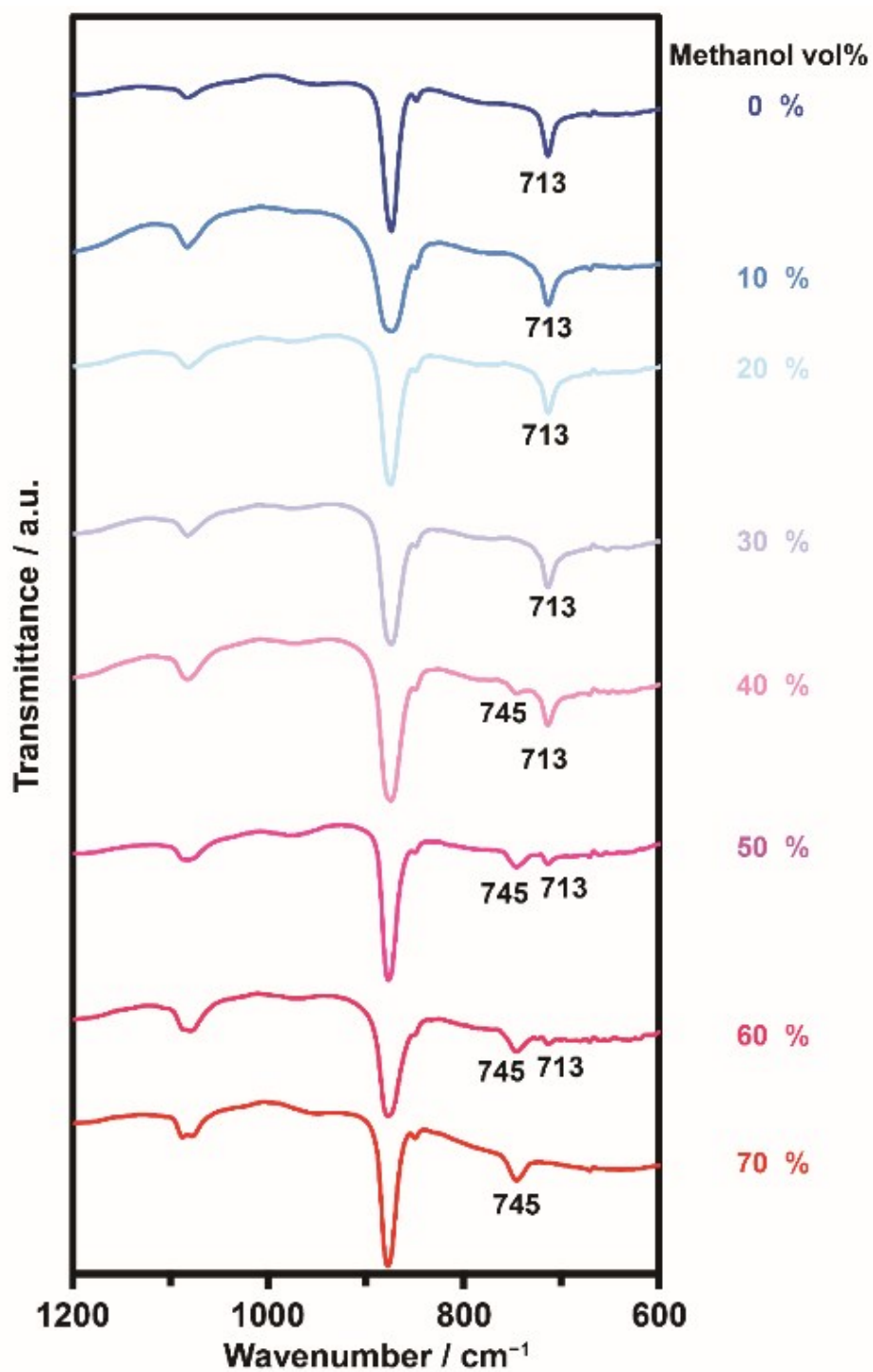


Fig. S13 FTIR spectra of nanocrystals obtained after crystallization of ACC precursors in solutions containing methanol volume fractions of 0%, 10%, 20%, 30%, 40%, 50%, 60%, and 70%.

The peaks at 713 cm⁻¹ were assigned to calcite. The peaks at 745 cm⁻¹ were attributed to vaterite.

Supporting references

1. S. R. Dickinson and K. M. McGrath, *Analyst*, 2001, **126**, 1118–1121.
2. F. A. Andersen and L. Brečević, *Acta Chem. Scand.*, 1991, **45**, 1018–1024.
3. I. C. Mcneill and S. M. T. Sadeghi, *Polym. Deg. Stab.*, 1990, **29**, 233–246.